INORGANIC CHEMISTRY FRONTIERS

RESEARCH ARTICLE

View Article Online
View Journal | View Issue

Cite this: *Inorg. Chem. Front.*, 2026, **13**, 95

Dynamic reconstruction of a pearl-thread-like CoS_2–Cu_xS interface for an enhanced oxygen evolution reaction

Heyang Liu,[a] Fengli Wei,[a] Linlin Huang,[a] Chenggong Niu,[a] Zuyang Luo,[a] Tayirjan Taylor Isimjan*[b] and Xiulin Yang *[a]

Received 12th August 2025,
Accepted 12th October 2025

DOI: 10.1039/d5qi01685a

rsc.li/frontiers-inorganic

Dynamic surface reconstruction offers a promising route to enhance oxygen evolution reaction (OER) activity by optimizing the adsorption of key intermediates. Here, we construct a pearl-thread-like CoS_2–Cu_xS heterostructure on copper foam (CoS_2–Cu_xS/CF) to induce *in situ* formation of an active CoOOH–CuO–Cu_xS interface at low potentials. *In situ* Raman spectroscopy confirms the dynamic transformation, while *operando* electrochemical impedance spectroscopy reveals accelerated charge transfer. Density functional theory calculations show that the interface engineering shifts the d-band center, enhances electron density near the Fermi level, and lowers the free energy barrier for *O to *OOH conversion from 1.78 eV (CoOOH) to 1.48 eV (CoOOH–CuO–Cu_xS). Benefiting from the reconstructed interface, CoS_2–Cu_xS/CF achieves an overpotential of 239 mV at 10 mA cm^{-2} and maintains stability for over 200 h in alkaline electrolyte. This work highlights a dynamic interface strategy to promote intrinsic OER kinetics and catalyst durability.

1. Introduction

The transition toward a sustainable energy future necessitates the development of efficient clean energy conversion technologies. Electrochemical water splitting has emerged as a promising route for carbon-neutral hydrogen production; however, its practical implementation is severely impeded by the sluggish kinetics of the oxygen evolution reaction (OER) at the anode.[1,2] The OER involves complex four-electron transfer steps and substantial energy barriers, particularly during the formation of O=O bonds, resulting in high overpotentials and poor energy efficiency.[3–5] Noble metal-based catalysts, such as RuO_2 and IrO_2, have been widely employed to mitigate these kinetic challenges by optimizing the adsorption energy of oxygenated intermediates.[6] Nevertheless, noble metals' limited availability and high cost severely restrict their widespread application in large-scale water splitting systems.[7]

To address these limitations, substantial efforts have focused on developing non-noble transition metal-based catalysts that are Earth-abundant and cost-effective and possess tunable electronic structures.[8,9] Among these, copper-based materials have garnered significant attention in OER systems due to their unique electronic configuration and high natural abundance. For instance, Zhu's group demonstrated that $CuNCo_3$ nanosheets achieved an overpotential of 260 mV at 10 mA cm^{-2}.[10] Chen's group electrodeposited CoS on $Cu(OH)_2$ nanorods to form three-dimensional hierarchical core–shell electrocatalysts, achieving an overpotential of 296 mV at the same current density.[11] However, Cu-based catalysts face inherent limitations, including high charge transfer resistance and sluggish reaction kinetics, which hinder their practical applications.[12] However, intrinsic drawbacks, including sluggish charge transfer kinetics and suboptimal binding energies for key OER intermediates, limit Cu-based materials' catalytic efficiency.[13,14]

Interface engineering has recently emerged as a powerful strategy to overcome these challenges by modulating the local electronic environment at heterostructured interfaces, thus enhancing electron transfer, tuning the d-band center, and facilitating optimal adsorption/desorption of oxygen species.[15,16] Dynamic surface reconstruction of catalysts during the OER process involves breaking intrinsic chemical bonds and *in situ* generation of high-valence metal hydroxide active phases, the "true catalytic species" for alkaline OER. In previous studies, Li *et al.* researched the transformation process of NiOOH in Ni(Fe) MOF.[17] Hao's group demonstrated that Ni(Fe)OOH species are the genuine active species for

[a]*Guangxi Key Laboratory of Low Carbon Energy Materials, School of Chemistry and Pharmaceutical Sciences, Guangxi Normal University, Guilin 541004, China. E-mail: xlyang@gxnu.edu.cn*
[b]*Saudi Arabia Basic Industries Corporation (SABIC) at King Abdullah University of Science and Technology (KAUST), Thuwal 23955-6900, Saudi Arabia. E-mail: isimjant@sabic.com*

FeOOH-modified $NiMoO_4$ electrodes.[18] While significant progress has been made in designing heterostructures for the OER, achieving dynamic surface reconstruction at low overpotentials to form catalytically active phases with strong interfacial electronic coupling remains an outstanding challenge.[19–21]

Herein, we report a self-supported, pearl-thread-like CoS_2–Cu_xS heterostructure grown on copper foam (CoS_2–Cu_xS/CF) that enables dynamic surface reconstruction under OER conditions. *In situ* Raman spectroscopy reveals the low-potential formation of a CoOOH–CuO–Cu_xS active interface through partial oxidation of CoS_2 and Cu_xS. *Operando* electrochemical impedance spectroscopy confirms enhanced charge transfer kinetics, and density functional theory (DFT) calculations show that the *in situ* generated interface optimizes the electronic structure, facilitating stronger *OOH adsorption and lowering the free energy barrier of the rate-determining step. Benefiting from the synergistic effects of dynamic reconstruction and interfacial coupling, the CoS_2–Cu_xS/CF catalyst exhibits outstanding OER performance with a low overpotential of 239 mV at 10 mA cm^{-2} and excellent operational stability for over 200 h in alkaline media. This study highlights the importance of interface design in promoting dynamic surface reconstruction and provides new insights into the rational design of high-performance, non-noble-metal OER catalysts.

2. Results and discussion

The synthesis pathway of CoS_2–Cu_xS/CF is illustrated in Fig. 1a. CoS_2–Cu_xS/CF was successfully synthesized through a straightforward one-step hydrothermal vulcanization method. During the preparation, copper foam (CF) with high electrical conductivity was selected as the substrate and copper source, while cobalt nitrate was the source of cobalt.[22] At elevated temperature and pressure, thiourea decomposes to generate hydrogen sulfide, which exhibits moderate reducing properties.[23,24] The resulting sulfide chemically reacts with metal ions, eventually growing CoS_2 and Cu_xS on the CF surface. The crystallographic structure of the obtained catalysts was characterized by X-ray diffraction (XRD). As shown in Fig. 1b, the diffraction peaks of Cu_xS/CF correspond to the standard cards for Cu (JCPDS: No. 85-1326), CuS (JCPDS: No. 78-0879), and Cu_2S (JCPDS: No. 84-0207). In addition to the Cu and Cu_xS phases, CoS_2–Cu_xS/CF exhibits peaks at 32.3, 36.2, and 39.8°, corresponding to CoS_2 (JCPDS: No. 89-1492). Compared with Cu_xS/CF, CoS_2–Cu_xS/CF displays peaks with higher intensity, indicating increased crystallinity upon CoS_2 incorporation. Raman spectroscopy was further employed to probe the vibrational modes of bonding sites on the catalyst surface (Fig. S1).[25,26] The peak at 267 cm^{-1} is assigned to the stretching vibration of the Cu–S bond, while the peak at 390 cm^{-1} corresponds to the Co–S bond. These results are consistent with XRD analysis, confirming the successful synthesis of CoS_2–Cu_xS/CF.[27] To further investigate the copper substrate's influence, we replaced CF with carbon cloth and synthesized samples under Cu-free conditions. The diffraction peaks of the resulting CoS_2–Co_3S_4/CC correspond to Co_2S (JCPDS No. 89-1492) and Co_3S_4 (JCPDS No. 75-1561). In contrast to CoS_2–Cu_xS/CF, the cobalt species in Co_2S–Co_3S_4/CC show a more complex phase composition, which can be attributed to the absence of copper during the reaction process (Fig. S2).

The morphology of CoS_2–Cu_xS/CF was characterized by scanning electron microscopy (SEM). As shown in Fig. S3a, the untreated copper foam (CF) exhibits a smooth surface. After hydrothermal treatment, CoS_2–Cu_xS/CF displays a uniformly distributed pearl-thread-like structure across the CF surface (Fig. 1c). Compared to the SEM image of Cu_xS/CF (Fig. S3b), introducing CoS_2 significantly improves the morphology, transforming it from a fragmented granular structure into an ordered pearly thread-like structure. This architecture provides a larger specific surface area and enhances the contact between the catalyst surface and the electrolyte, thereby promoting OER activity.[28] To further investigate the morphological evolution during synthesis, we monitored the catalyst structure as a function of hydrothermal reaction time (Fig. S4). Initially, only a few thread-like features were observed within 2 h. With a prolonged reaction time, these structures gradually developed into more ordered pearl-thread-like formations. However, after 4 h, excessive growth led to the appearance of aggregated granular structures that covered the underlying framework. These observations suggest that insufficient and excessive hydrothermal durations are detrimental to the formation of the optimal morphology, limiting active site exposure and hindering the adsorption of reactive oxygen species.[29]

Transmission electron microscopy (TEM) and high-angle annular dark-field scanning transmission electron microscopy (HAADF-STEM) were further employed to visualize the structure in greater detail. As shown in Fig. 1d, TEM confirms the distinctive pearl-thread morphology observed in SEM. High-resolution TEM (HR-TEM) images (Fig. 1e) reveal dual lattice fringes with spacings of 0.247, 0.291, and 0.265 nm, corresponding to the (210) plane of CoS_2, the (112) plane of Cu_2S, and the (107) plane of CuS, respectively (Fig. 1f). Selected area electron diffraction (SAED) patterns (Fig. 1g) further corroborate these assignments, indicating a polycrystalline structure. Elemental analysis through energy-dispersive X-ray spectroscopy (EDX) (Fig. S5) and energy-dispersive spectroscopy (EDS) elemental mapping (Fig. 1h) reveals a homogeneous distribution of Co, Cu, and S throughout the structure. Together, these comprehensive characterization studies confirm the successful construction of the CoS_2–Cu_xS/CF catalyst.

The surface elemental composition and valence states are explored by X-ray photoelectron spectroscopy (XPS). The high-resolution C 1s spectrum of CoS_2–Cu_xS/CF is employed as a calibration standard for other elements (Fig. S6). The peaks at around 284, 284.8, 286, and 288.4 eV are assigned to C═C, C–C, C–O, and C═O, respectively.[30] The high-resolution Cu 2p spectrum demonstrated two peaks centered at 932.6 eV and 933.6 eV, assigned to Cu^+ and Cu^{2+} in CoS_2–Cu_xS/CF (Fig. 2a).[31] Compared with Cu_xS/CF, the Cu^+ peak in CoS_2–

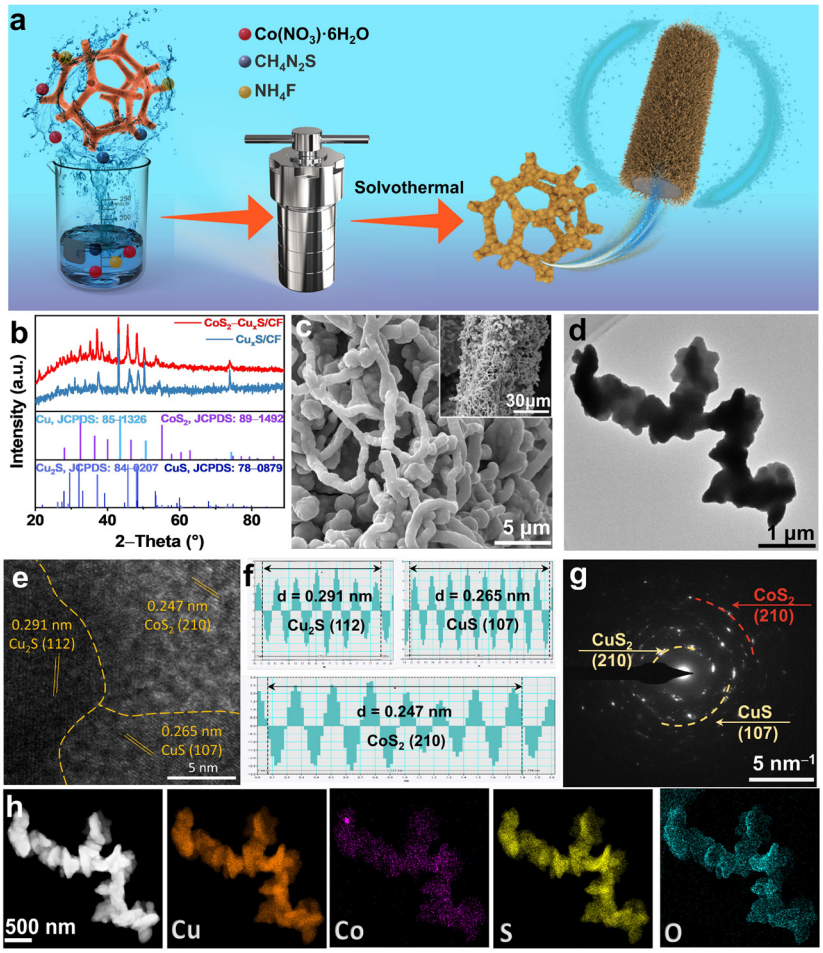

Fig. 1 (a) Schematic illustration of the preparation of CoS_2–Cu_xS/CF. (b) XRD patterns. (c) SEM image. (d) TEM image. (e) HR-TEM image. (f) Corresponding lattice spacing profiles. (g) SAED pattern. (h) HAADF-STEM image and corresponding elemental maps of CoS_2–Cu_xS/CF.

Cu_xS/CF shifts 0.5 eV towards lower binding energy, accompanied by an increased Cu^+/Cu^{2+} ratio. This indicates that CoS_2 alters the local electronic environment of Cu_xS, facilitating the conversion of Cu^+ into Cu^{2+} and accelerating the generation of active intermediates. Given the close binding energies of Cu^0 and Cu^+, Cu LMM Auger spectra were also collected (inset of Fig. 2a).[32] A peak at 569.2 eV corresponds to Cu^+, while a peak at 566.5 eV is attributed to Cu^0, confirming the oxidation states.[33]

Within the S 2p spectral range for CoS_2–Cu_xS/CF (Fig. 2b), the characteristic peaks at 161.6 and 162.3 eV are assigned to S $2p_{3/2}$ and S $2p_{1/2}$, with essentially no changes in the electronic environment.[34] For the spectra of Co 2p, the peak at 778.4 eV corresponds to Co–S, while 781.5 and 784.2 eV are ascribed to Co^{2+} and satellite peaks, demonstrating that the cobalt is mainly present in the form of Co^{2+} for CoS_2–Cu_xS/CF (Fig. 2c).[35,36] Based on the comprehensive analysis of XPS results, the valence shift of Cu and the retention of S valence indicate electron transfer between CoS_2 and Cu_xS, which improves the metal coordination environment, thus enhancing catalytic efficiency. Besides, we performed contact angle tests to investigate the impact of interfacial interactions on water adhesion. As shown in Fig. 2d, CoS_2–Cu_xS/CF exhibits a contact angle of 29.2°, much smaller than the 56.4° of Cu_xS/CF, meaning more intimate contact between the catalytic surface and electrolyte for the CoS_2–Cu_xS heterostructure, which modifies the catalyst surface wettability, promoting the transportation of the catalyst to the electrolyte.[37]

The OER performance of CoS_2–Cu_xS/CF was evaluated in 1.0 M KOH using a standard three-electrode system. As shown in Fig. 3a, CoS_2–Cu_xS/CF exhibits outstanding activity, requiring an overpotential of only 239 mV at 10 mA cm^{-2} and 315 mV at 100 mA cm^{-2}. Compared with CoS_2–Co_3S_4/CC and Cu_xS/CF, CoS_2–Cu_xS/CF demonstrates superior catalytic performance, surpassing even RuO_2/CF (η = 259 mV at 10 mA cm^{-2}) under alkaline conditions. Notably, a high current density of 500 mA cm^{-2} is achieved with a relatively low overpotential of 390 mV, demonstrating the potential of CoS_2–Cu_xS/CF for high-current-density applications. Tafel plots (Fig. 3b) highlight the favorable reaction kinetics of CoS_2–Cu_xS/CF, with a Tafel slope of 60.3 mV dec^{-1}, significantly lower than those of CoS_2–Co_3S_4/CC (71.7 mV dec^{-1}) and Cu_xS/

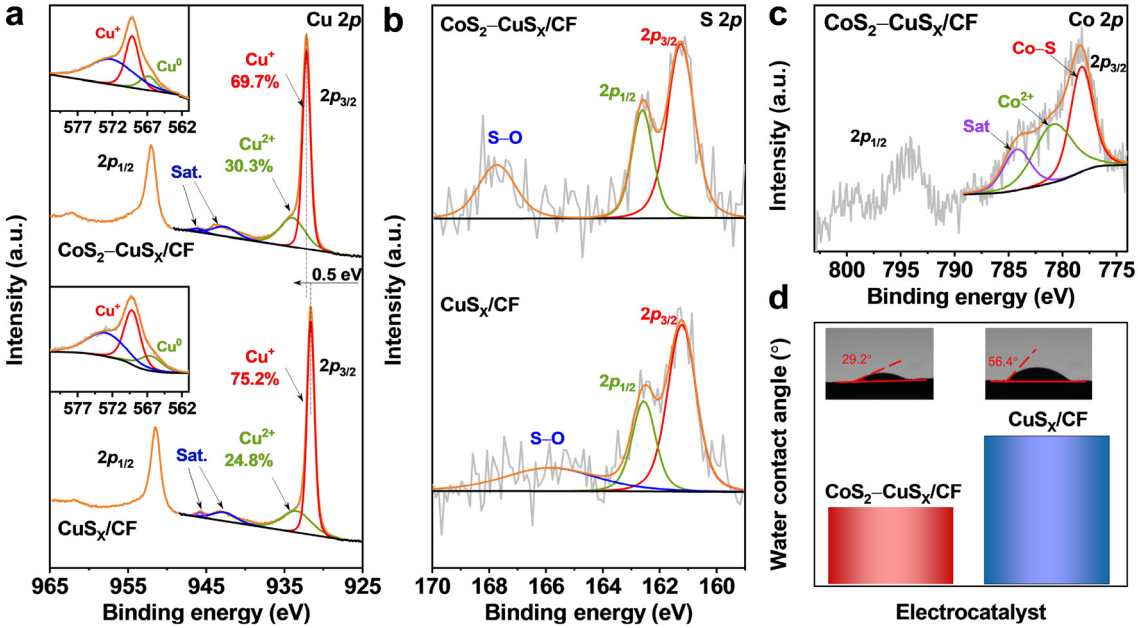

Fig. 2 High-resolution XPS spectra of (a) Cu 2p (the inset shows Cu LMM Auger spectra) and (b) S 2p regions in CoS_2–Cu_xS/CF and Cu_xS/CF. (c) Co 2p of CoS_2–Cu_xS/CF. (d) Contact angle images of CoS_2–Cu_xS/CF and Cu_xS/CF.

CF (96.7 mV dec^{-1}), indicating accelerated charge transfer and reduced energy loss during the OER.[38,39] The catalytic performance of CoS_2–Cu_xS/CF is influenced by synthetic parameters such as the amount of $Co(NO_3)_2$, hydrothermal time, and temperature. Optimization studies (Fig. S7) reveal that using 1.5 mmol $Co(NO_3)_2$ achieves the best performance, with faster reaction kinetics and improved charge transfer (Fig. S7). Further investigations (Fig. S8 and S9) show that a hydrothermal time of 4 h and a temperature of 150 °C yield the optimal morphology and catalytic activity. The enhanced performance is attributed to the synergistic effects between CoS_2 and Cu_xS, which improve interfacial electron transfer and facilitate dynamic surface reconstruction by reducing charge transfer resistance (R_{ct}). Additional cyclic voltammetry (CV) analyses supporting these observations are shown in Fig S10–S12. As summarized in Fig. 3c and Table S2, CoS_2–Cu_xS/CF ranks among the best-performing sulfide and copper-based OER catalysts reported. The double-layer capacitance (C_{dl}) obtained from CV measurements (Fig. 3d) indicates the electrochemical surface area.[40] The C_{dl} for CoS_2–Cu_xS/CF is 93.2 mF cm^{-2}, surpassing the comparison samples by several times, such as Cu_xS/CF (28.6 mF cm^{-2}), CoS_2–Co_3S_4/CC (20.4 mF cm^{-2}), and CF (19.7 mF cm^{-2}). The electrochemical surface area (ECSA) is determined using C_{dl} (Fig. 3e). A specific capacitance of 40 mF cm^{-2} is selected under normal circumstances.[41] The electrochemical surface area (ECSA) is calculated to be 1560 cm^2 for CoS_2–Cu_xS/CF, nearly five times larger than that of Cu_xS/CF (340 cm^2) (Fig. 3e). The pearl-thread-like morphology is responsible for the expanded surface area, increasing active site exposure and enhancing catalyst–electrolyte interactions.[42] The larger specific surface increases the exposure of the interface in solution, which achieves higher density interfaces and facilitates the bonding of the active site. In order to demonstrate the intrinsic activity of CoS_2–Cu_xS/CF more efficiently, ECSA-normalized LSV curves are displayed in Fig. 3e as well, which prove that CoS_2–Cu_xS/CF has the highest electrocatalytic performance and intrinsic activity for the OER in an alkaline environment. The turnover frequency (TOF) is derived from the results of inductively coupled plasma mass spectrometry (ICP-MS), invariably correlating with the intrinsic activity of electrocatalysts (Table S1).[43] As depicted in Fig. 3f, the TOF of CoS_2–Cu_xS/CF exhibits the most rapid increasing trend with rising applied voltage. When the applied voltage reaches 259 mV, the TOF value of CoS_2–Cu_xS/CF is 0.03 s^{-1}, further demonstrating that the formation of the CoS_2–Cu_xS interface improves the intrinsic activity. The faradaic efficiency (FE) of the OER process is further calculated, representing the ratio of actual gas evolved to the theoretical amount (Fig. 3g).[44] As a result, actual oxygen production and theoretical oxygen production exhibit an extremely high degree of fit. More than 10 mL of O_2 is generated by 1 cm^2 of CoS_2–Cu_xS/CF within 30 min, which is close to the theoretical oxygen production. In particular, the high activity of CoS_2–Cu_xS/CF can be maintained for over 200 h at a current density of 100 mA cm^{-2} (Fig. 3h), implying the extraordinary cycling stability of CoS_2–Cu_xS/CF.

The surface evolution of CoS_2–Cu_xS/CF during the OER process was investigated using transmission electron microscopy (TEM) after long-term stability testing. As shown in Fig. S13 and 14, the reaction process induced significant alterations in the microscopic morphology of the catalyst surface. Additionally, high-angle annular dark-field scanning

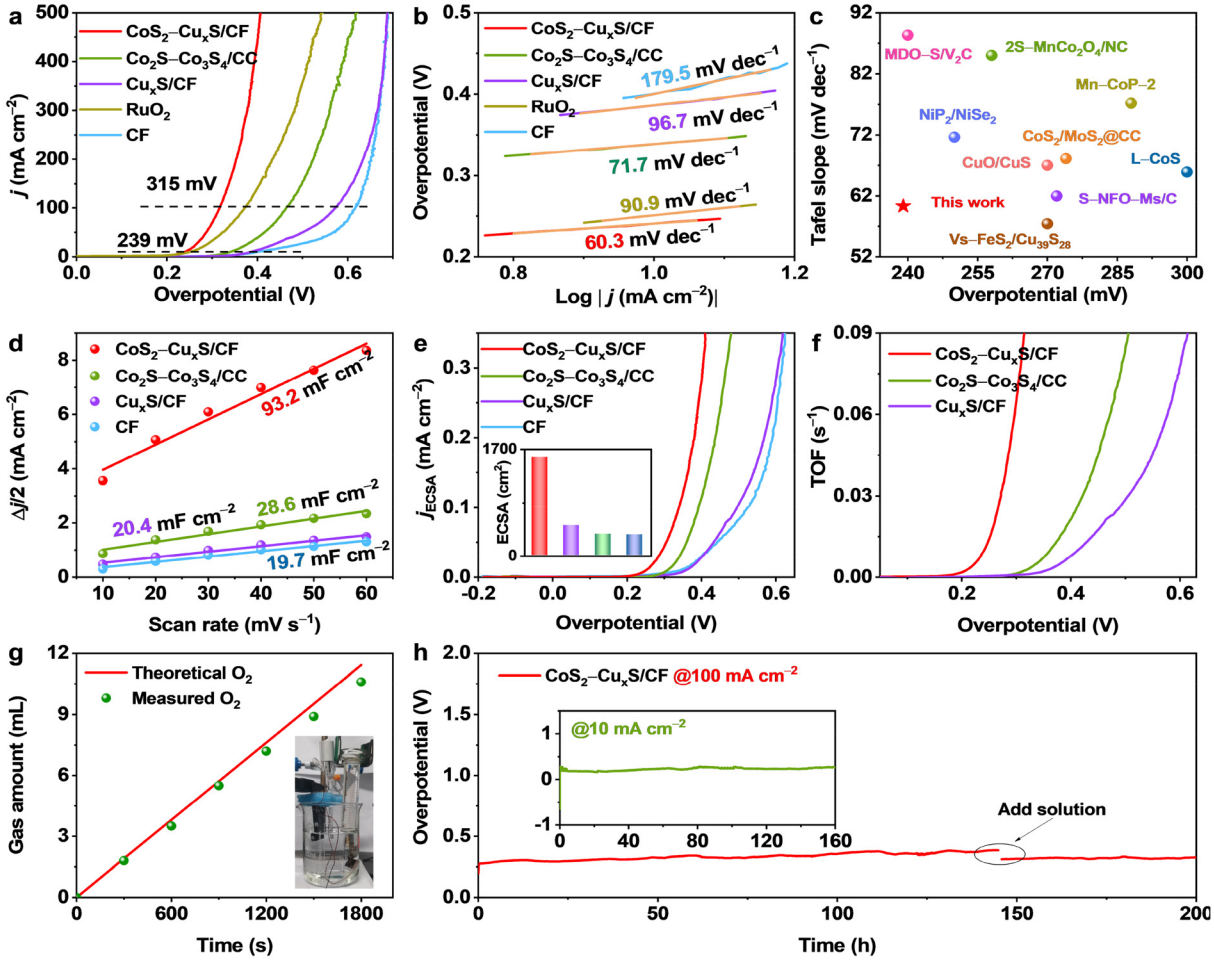

Fig. 3 (a) LSV curves. (b) Tafel plots. (c) Comparison of overpotentials at 10 mA cm^{-2} and Tafel slopes for previously reported catalysts. (d) C_{dl} plots. (e) ECSA-normalized LSV curves (the inset shows the comparison of ECSAs for different catalysts). (f) TOF curves. (g) Faradaic efficiency measurement for the OER. (h) Stability test at 100 mA cm^{-2} (the inset shows the stability test at 10 mA cm^{-2}).

TEM (HAADF-STEM) combined with energy-dispersive X-ray (EDX) mapping revealed the uniform distribution of Cu, Co, O, and S throughout the structure (Fig. S15 and S16), further validating the catalyst's composition and architecture after the reaction. Notably, the oxygen content increased significantly after the OER process, accompanied by a corresponding decrease in sulfur content, implying the partial transformation of sulfides into oxides. TEM analysis revealed a lattice fringe spacing of 0.186 nm, corresponding to the (202) plane of CuO, confirming the formation of CuO (Fig. 4a and b). Additionally, a spacing of 0.230 nm is assigned to the (006) plane of CoOOH, indicating the generation of CoOOH during the OER. These findings are consistent with post-reaction XPS analysis (Fig. 4c), where an increase in the Cu^{2+} signal corroborates the formation of CuO. In addition, residual sulfur signals were still detected by XPS (Fig. 4d), which may have come from residual SO_4^{2-}. To verify this, a residual SO_4^{2-} detection experiment was conducted (Fig. S17). The reacted catalyst was placed in deionized water and subjected to 12 h of ultrasonic treatment. Then, the solution was acidified with dilute hydrochloric acid, and $BaCl_2$ solution was added. The result showed that a small amount of white precipitate appeared, indicating the presence of residual SO_4^{2-} on the surface of the catalyst after the reaction.[45]

In situ Raman spectroscopy was further employed to monitor structural evolution during the OER. Compared to the dry state, Raman scattering peaks at 390 cm^{-1} weakened after immersion in alkaline electrolyte due to environmental changes. In addition, copper foam (CF) oxidizes readily upon exposure to water, leading to observable Cu–O vibrations at open-circuit potential (OCP). As shown in Fig. 4e, characteristic Raman peaks at 270 cm^{-1}, 348 cm^{-1}, and 550 cm^{-1} correspond to Cu–O, Cu–S, and CoOOH, respectively.[25,26,46] With increasing applied potential, the intensity of the Cu–S peak gradually decreases, while the Cu–O peak intensifies, indicating progressive oxidation of Cu_xS. Importantly, CoOOH formation becomes significant only after substantial CuO generation, suggesting that the disruption of the Cu–S bond and the formation of Cu–O bonds redistribute the local charge density, thereby facilitating the activation of Co sites into

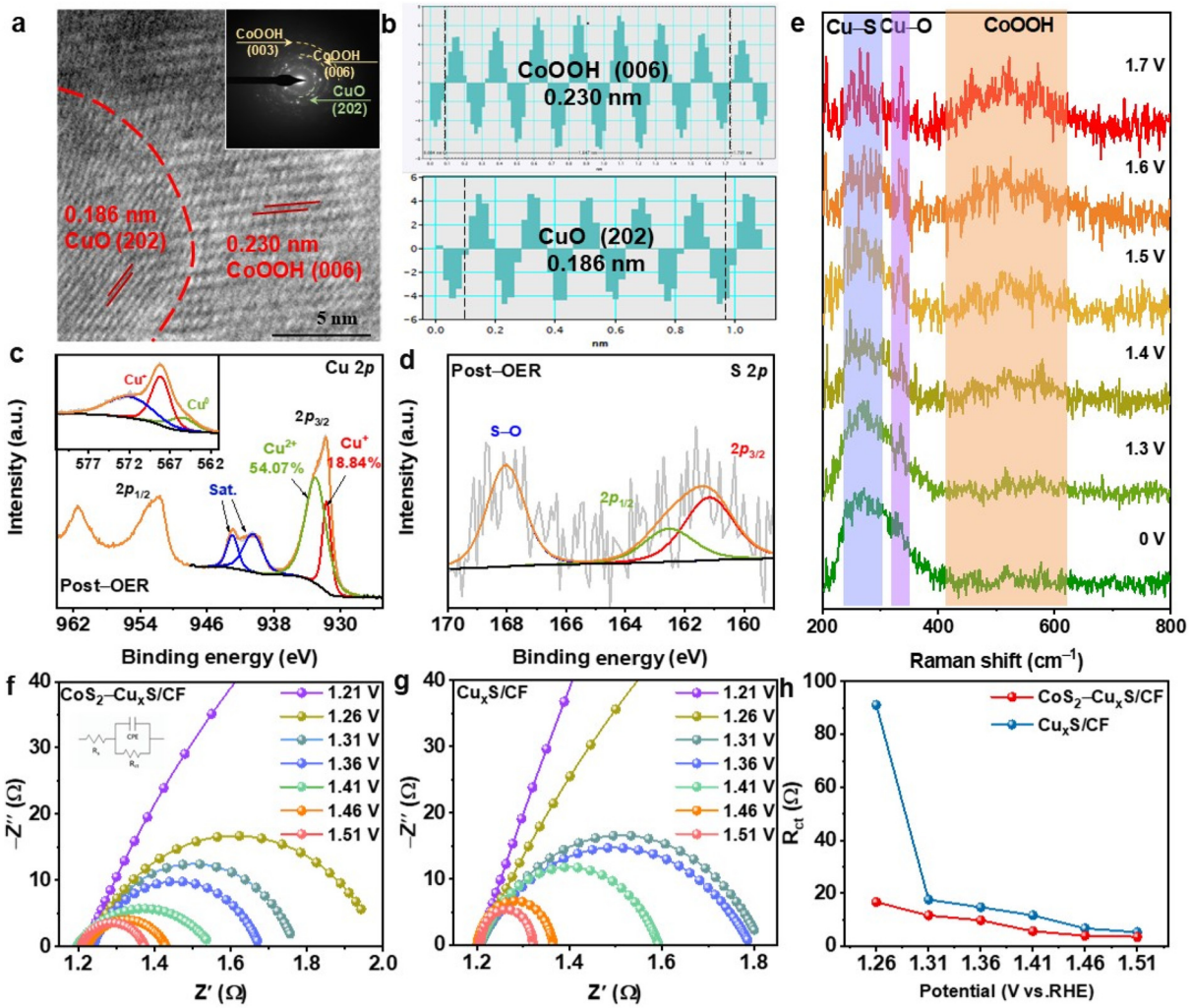

Fig. 4 (a and b) TEM image of CoS_2–Cu_xS/CF after the reaction. High-resolution XPS spectra of (c) Cu 2p (the inset shows Cu LMM Auger spectra) and (d) S 2p regions in CoS_2–Cu_xS/CF and Cu_xS/CF after the reaction. (e) Potential-dependent *in situ* Raman spectra of CoS_2–Cu_xS/CF at different potentials (*vs.* RHE). Nyquist plots for (f) CoS_2–Cu_xS/CF and (g) Cu_xS/CF at different applied potentials (*vs.* RHE). (h) Variation trend of R_{ct} under different potentials for CoS_2–Cu_xS/CF and Cu_xS/CF.

highly active CoOOH species. As shown in Fig. S18, the Raman peaks at 470 and 527 cm^{-1} belong to Co–S.[47] As the applied voltage increases, the signal corresponding to Co–S disappears. When the voltage rises to 1.5 V, a characteristic peak attributed to CoOOH begins to emerge. The overpotential required for the surface reconstruction of the single CoS_2 interface is much higher than that of the CoS_2–Cu_xS interface, which indicates that the CoS_2–Cu_xS heterostructure promotes the adsorption of OH^- onto active intermediates, effectively improving the reaction kinetics. Combined analysis of these results confirms that a CoOOH–CuO–Cu_xS heterointerface forms during the OER process. CoS_2 and Cu_xS are partially transformed into CoOOH and CuO, respectively. This hybrid structure benefits from the high conductivity of residual sulfides, lowering charge transfer resistance and enhancing reaction kinetics. Notably, *in situ* Raman spectroscopy showed that the Cu–S bond did not disappear even when the applied voltage reached 1.7 V, indicating the presence of residual CuS_x. In summary, the *in situ* generated CoOOH–CuO–Cu_xS interface replaces the original sulfide phase, significantly boosting catalytic activity.[48]

Electrochemical impedance spectroscopy (EIS) was performed to further investigate the dynamic evolution of active species on the catalyst surface.[49] *In situ* EIS measurements are conducted at various potentials to further elucidate the role of Co sites in promoting the adsorption and desorption of oxygen-containing reactants.[50] Fig. 4f and g and present the Nyquist plots of CoS_2–Cu_xS/CF and Cu_xS/CF at different potentials. As the potential increased, the charge transfer resistance (R_{ct}) decreased significantly, indicating a notable acceleration in reaction kinetics.[51] Moreover, the charge transfer rate of CoS_2–Cu_xS/CF is consistently higher than that of Cu_xS/CF, which can be attributed to the dynamic evolution of Co sites at the interfaces of the Cu_xS and CoS_2 species. The relevant bond

plots are presented in Fig. S19. As the applied voltage increases, the position of the phase angle changes continuously, which reveals that the phase angles of CoS_2–CuS_x are smaller than those of CuS_x at each identical applied potential. This indicates that more electrons participate in OER catalysis, thereby enhancing the kinetics of the OER. Fig. 4h illustrates the decreasing trend of R_{ct} between CoS_2–Cu_xS/CF and Cu_xS/CF. Under low-potential conditions, the Co active sites exhibit enhanced adsorption of oxygen-containing intermediates. These intermediates are rapidly accumulated upon the introduction of the Co sites, activating the OER performance of catalysts at low potentials.[52]

To elucidate electronic interactions of key reaction intermediates at the interface, we modeled the system using density functional theory (DFT).[53] To align with system characterization, CoOOH–CuO–Cu_xS is selected as the computational model, with CoOOH serving as the contrast sample. Fig. 5a shows the optimized model configuration. The differential charge density is analyzed in Fig. 5b, with the yellow region indicating electron accumulation and the green region representing electron depletion. This suggests that there is localized charge accumulation near CoOOH and CuO regions. Significantly, charge aggregation at Cu sites is markedly weaker than that at Co sites, implying that CuO regulates interfacial electron transfer.[54] This electronic coupling is further clarified in the two-dimensional charge density projection (Fig. 5c), where the blue region represents electron accumulation, and the red region indicates electron depletion. Density of states (DOS) calculations (Fig. 5d) reveal enhanced electron density near the Fermi level for CoOOH–CuO–Cu_xS compared to CoOOH, demonstrating that CoOOH–CuO interactions promote interfacial electron mobility and improve material conductivity.[55] The d-band center shifts from −1.27 eV (CoOOH) to −1.17 eV (CoOOH–CuO–Cu_xS), indicating higher antibonding orbital occupancy above the Fermi level and reduced bonding orbital occupancy below the Fermi level

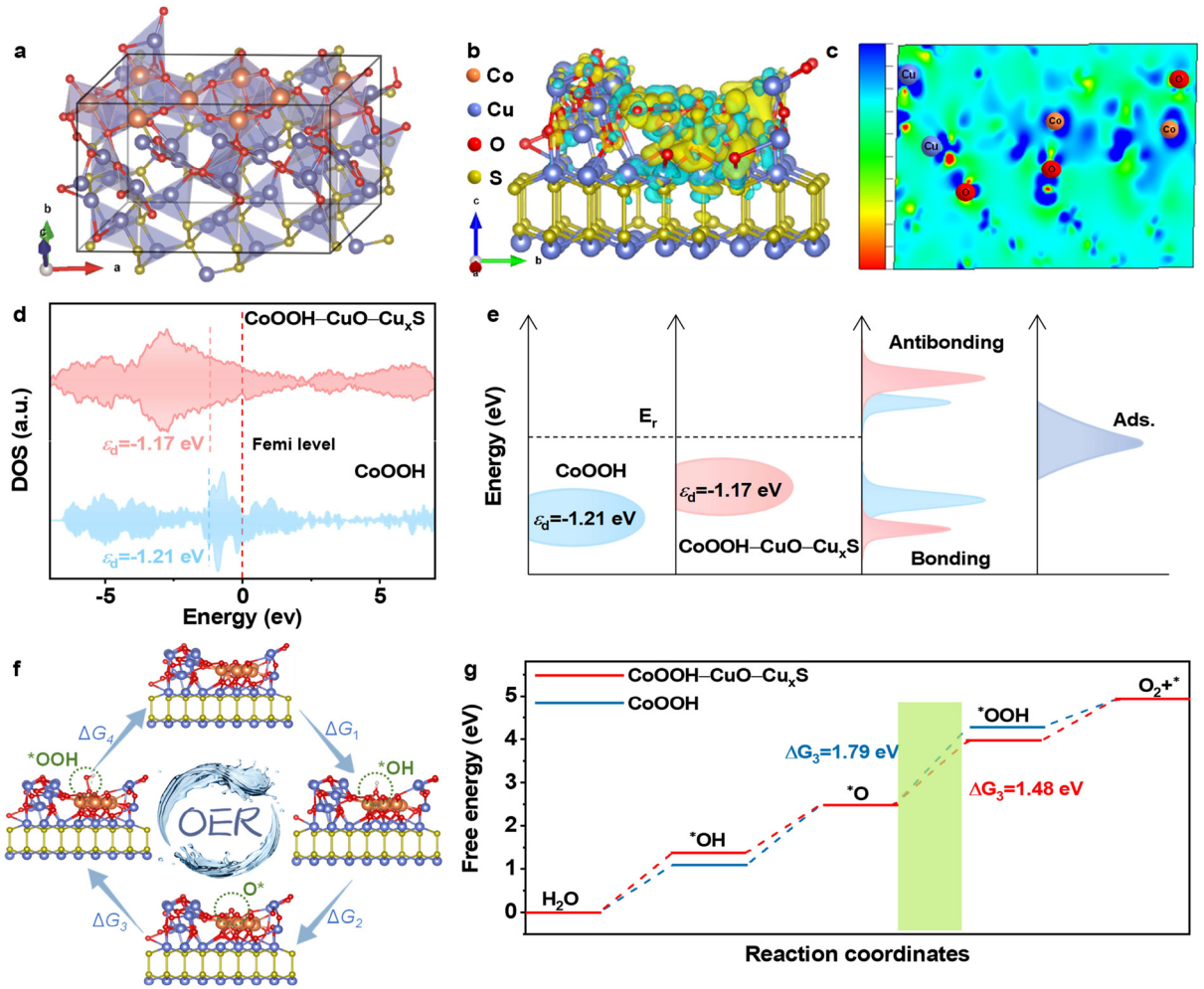

Fig. 5 (a) Optimized model configuration. (b) Charge density difference of CoOOH–CuO–Cu_xS. (c) Cross-sectional diagram. (d) DOS for CoOOH–CuO–Cu_xS and CoOOH. (e) Schematic representation of the d-band center and the electronic interaction governing bond formation between the catalyst surface and the adsorbate. (f) OER mechanism illustration of CoOOH–CuO–Cu_xS. (g) Gibbs free energy diagrams of CoOOH–CuO–Cu_xS and CoOOH.

(Fig. 5e), which is consistent with weakened Co–O bonds that favor oxygen species desorption.[56] Fig. 5f illustrates the four-electron OER pathway on CoOOH–CuO–Cu_xS, where Co sites remain the primary adsorption centers. Hydroxide adsorption forms *OH intermediates on Co sites, followed by sequential deprotonation to *O and *OOH species, culminating in O_2 release.[57] Gibbs free energy (ΔG) analysis (Fig. 5g) identifies the transition from *O to *OOH (ΔG_3) as the rate-determining step. CoOOH–CuO–Cu_xS exhibits a significantly lower ΔG_3 (1.48 eV) compared to CoOOH (1.79 eV), which reduces energy barriers of *O to *OOH, further facilitating the formation of CoOOH. In summary, compared to single CoOOH, the *in situ* generated active CoOOH–CuO–Cu_xS interfaces optimize the electronic structure and facilitate the desorption of oxygen-containing intermediates *O during the OER process, resulting in excellent OER performance.

The excellent OER performance motivates us to apply the catalyst in overall water splitting. Fig. S20a shows the model of the overall water splitting device. Electrochemical analyses revealed that the CoS_2–Cu_xS/$CF^{(+)}$||Pt/$C^{(-)}$ system demonstrated superior overall water splitting performance relative to the control in 1.0 M KOH. As shown in the polarization curve (Fig. S20b), the CoS_2–Cu_xS/$CF^{(+)}$||Pt/$C^{(-)}$ electrolyzer required only 1.62 V to achieve a current density of 100 mA cm^{-2}, substantially lower than the 1.82 V required for the $RuO_2^{(+)}$||Pt/$C^{(-)}$ system. Furthermore, the CoS_2–Cu_xS/$CF^{(+)}$||Pt/$C^{(-)}$ system exhibited competitive performance at 100 mA cm^{-2} compared with numerous reported electrocatalysts (Fig. S20c and Table S3). As demonstrated in Fig. S20d, the CoS_2–Cu_xS/$CF^{(+)}$||Pt/$C^{(-)}$ system exhibits outstanding stability at a current density of 100 mA cm^{-2} for over 60 h, indicating its certain potential for industrial applications.

3. Conclusion

We developed a self-supported CoS_2–Cu_xS/CF electrocatalyst that undergoes dynamic surface reconstruction to form an active CoOOH–CuO–Cu_xS interface under OER conditions. *In situ* and *operando* characterization studies, supported by DFT calculations, reveal that the engineered interface enhances electronic coupling, optimizes *OOH adsorption, and reduces the rate-determining step barrier by 0.30 eV compared to pristine CoOOH. As a result, CoS_2–Cu_xS/CF delivers a low overpotential of 239 mV at 10 mA cm^{-2}, a high current density of 500 mA cm^{-2} at 390 mV, and long-term stability exceeding 200 h. These findings underscore the significance of dynamic interface design in advancing non-noble-metal OER catalysts for sustainable water splitting applications.

Author contributions

Heyang Liu: writing – original draft and methodology. Fengli Wei: validation and investigation. Linlin Huang: methodology. Chenggong Niu: validation. Zuyang Luo: investigation. Tayirjan Taylor Isimjan: writing – review & editing. Xiulin Yang: writing – review & editing and supervision.

Conflicts of interest

The authors declare no conflict of interest.

Data availability

The data supporting this article have been included as part of the supplementary information (SI). Supplementary information is available. See DOI: **https://doi.org/10.1039/d5qi01685a**.

Acknowledgements

This work has been supported by the National Natural Science Foundation of China (no. 52363028, 21965005), the Natural Science Foundation of Guangxi Province (2021GXNSFAA076001, 2018GXNSFAA294077), and the Guangxi Training Program of Innovation and Entrepreneurship for Undergraduates (S202410602138).

References

1 Q. Li, W. Luo, X. Cui and J. Shi, Rapid and In Situ Active Sites Regeneration for OER Activity Recovery and Greatly Prolonged Water-Splitting Performance, *Angew. Chem., Int. Ed.*, 2025, e202500303.
2 X. Li, J. Wang, H. Xue, L. Zhao, J. Lu, H. Zhang, M. Yan, F. Deng and C. Hu, Tuning α-MnOOH Formation via Atomic-Level Fe Introduction for Superior OER Performance, *Adv. Funct. Mater.*, 2025, 2503360.
3 X. Cui, T. Tang, F. Zhang, L. Sun and B. Zhang, New benchmark for pure nickel-based oxygen-evolution electrocatalyst: Tailored large NiMoO4·xH_2O monocrystals for complete reconstruction, *Appl. Catal., B*, 2025, **366**, 125024.
4 Y. Zhu, Z. Cai, Q. Wei, R. Chen, F. Guo, Y. Jiang, Y. Xiao, J. Guo, Z. Wang, J. Zhong and N. Cheng, Asymmetric Electron Transport-Induced Formation of High-Valent IrO_x in NiFeOOH Heterostructure for Efficient Water Oxidation, *Adv. Funct. Mater.*, 2025, 2503692.
5 Y. Li, Z. Zhang, Z. Zhang, J. He, M. Xie, C. Li, H. Lu, Z. Shi and S. Feng, Construction of Ni_2P-$NiFe_2O4$ heterostructured nanosheets towards performance-enhanced water oxidation reaction, *Appl. Catal., B*, 2023, **339**, 123141.
6 Y. Sun, J. Chen, L. Liu, H. Chi and H. Han, The mechanism of OER activity and stability enhancement in acid by atomically doped iridium in γ-MnO_2, *Chin. J. Catal.*, 2025, **69**, 99–110.
7 B. Guo, W. Li, H. Chen, H. Zhang, H. Li, X. Feng, B. Li, L. Wang, Z. Wang and Z. Kou, Single-atom Ru anchored on Co_3S_4 nanowires enabling ampere-level water splitting for

multi-scenarios green energy-to-hydrogen systems, *Nano Energy*, 2025, **138**, 110881.

8 L. He, N. Wang, M. Xiang, L. Zhong, S. Komarneni and W. Hu, S-vacancy-rich NiFe-S nanosheets based on a fully electrochemical strategy for large-scale and quasi-industrial OER catalysts, *Appl. Catal., B*, 2024, **345**, 123686.

9 C. Jing, L. Li, Y.-Y. Chin, C.-W. Pao, W.-H. Huang, M. Liu, J. Zhou, T. Yuan, X. Zhou, Y. Wang, C.-T. Chen, D.-W. Li, J.-Q. Wang, Z. Hu and L. Zhang, Balance between FeIV–NiIV synergy and Lattice Oxygen Contribution for Accelerating Water Oxidation, *ACS Nano*, 2024, **18**(22), 14496–14506.

10 L. Zhu, C. Li, H. Li, H. Li, Z. Wu, Y. Huang, X. Zhu and Y. Sun, Adjustable antiperovskite cobalt-based nitrides as efficient electrocatalysts for overall water splitting, *J. Mater. Chem. A*, 2022, **10**(29), 15520–15527.

11 Y. Chen, Q. Zhao, Y. Zhou, L. Liu and T. Jiang, Hierarchical core-shell $Cu(OH)_2$@CoS/CF nanoarrays for electrocatalytic water oxidation, *J. Alloys Compd.*, 2023, **935**, 167857.

12 T. A. Shifa, A. Gradone, K. Yusupov, K. B. Ibrahim, M. Jugovac, P. M. Sheverdyaeva, J. Rosen, V. Morandi, P. Moras and A. Vomiero, Interfacing CrO_x and CuS for synergistically enhanced water oxidation catalysis, *Chem. Eng. J.*, 2023, **453**, 139781.

13 F. N. I. Sari, Y.-C. Lai, Y.-J. Huang, X.-Y. Wei, H. Pourzolfaghar, Y.-H. Chang, M. Ghufron, Y.-Y. Li, Y.-H. Su, O. Clemens and J.-M. Ting, Electronic Structure Engineering in NiFe Sulfide via A Third Metal Doping as Efficient Bifunctional OER/ORR Electrocatalyst for Rechargeable Zinc-Air Battery, *Adv. Funct. Mater.*, 2024, **34**(21), 2310181.

14 Y.-j. Wu, J. Yang, T.-x. Tu, W.-q. Li, P.-f. Zhang, Y. Zhou, J.-f. Li, J.-t. Li and S.-G. Sun, Evolution of Cationic Vacancy Defects: A Motif for Surface Restructuration of OER Precatalyst, *Angew. Chem., Int. Ed.*, 2021, **60**(51), 26829–26836.

15 J. Jia, Y. Wang, Y. Cha, Z. Wang, J. Huang, D. Wang, H. Li, K. Guo, J. Li, J. Huang, Y. Tang and C. Xu, Boosting OER Performance of NiFe-MOFs via Heterostructure Engineering: Promoted Phase Transformation and Self-optimized Dynamic Interface Electron Structure, *Adv. Funct. Mater.*, 2025, 2500568.

16 D. Chanda, H. Kwon, M. M. Meshesha, J. S. Gwon, M. Ju, K. Kim and B. L. Yang, Modulating interfacial electronic coupling of copper-mediated NiFe layered double hydroxide nanoprisms via structural engineering for efficient OER in wireless photovoltaic-coupled and anion exchange membrane water electrolysis, *Appl. Catal., B*, 2024, **340**, 123187.

17 Y. Li, L. Yang, X. Hao, X. Xu, L. Xu, B. Wei and Z. Chen, Origin of Enhanced Oxygen Evolution in Restructured Metal–Organic Frameworks for Anion Exchange Membrane Water Electrolysis, *Angew. Chem., Int. Ed.*, 2024, **64**, e202413916.

18 H. Hao, J. Wang, Z. Wang, S. Shen, L. Xu, Z. Lv and B. Wei, Elucidating the superwetting FeOOH-modified $NiMoO_4$ electrodes for efficient alkaline oxygen evolution reaction: An *in situ* spectroscopy study, *Appl. Catal., B*, 2025, **363**, 124814.

19 X. Xu, K. Guo, J. Sun, X. Yu, X. Miao, W. Lu and L. Jiao, Interface Engineering of Mo-doped Ni_2P/Fe_xP-V Multiheterostructure for Efficient Dual-pH Hydrogen Evolution and Overall Water Splitting, *Adv. Funct. Mater.*, 2024, **34**(33), 2400397.

20 Y. Lin, Y. Pan, S. Liu, K. Sun, Y. Cheng, M. Liu, Z. Wang, X. Li and J. Zhang, Construction of multi-dimensional core/shell Ni/NiCoP nano-heterojunction for efficient electrocatalytic water splitting, *Appl. Catal., B*, 2019, **259**, 118039.

21 C. Xu, Y. Hong, Z. Li, X. Di, W. Wang, X. Dong and X. Mou, Transition metal-based heterojunctions for alkaline electrocatalytic water splitting, *Coord. Chem. Rev.*, 2025, **523**, 216287.

22 C. Li, B. Zhang, Y. Li, S. Hao, X. Cao, G. Yang, J. Wu and Y. Huang, Self-assembled Cu-Ni bimetal oxide 3D in-plane epitaxial structures for highly efficient oxygen evolution reaction, *Appl. Catal., B*, 2019, **244**, 56–62.

23 F. Wei, J. Shen, J. Xie, Z. Luo, L. Shi, T. T. Isimjan, X. Yang, J. Qiu and B. Wu, Dynamic in situ reconstruction of $NiSe_2$ promoted by interfacial $Ce_2(CO_3)_2O$ for enhanced water oxidation, *J. Energy Chem.*, 2024, **98**, 472–480.

24 K. Jayaramulu, J. Masa, O. Tomanec, D. Peeters, V. Ranc, A. Schneemann, R. Zboril, W. Schuhmann and R. A. Fischer, Nanoporous Nitrogen-Doped Graphene Oxide/Nickel Sulfide Composite Sheets Derived from a Metal-Organic Framework as an Efficient Electrocatalyst for Hydrogen and Oxygen Evolution, *Adv. Funct. Mater.*, 2017, **27**(33), 1700451.

25 J. Zhu, S. Zi, N. Zhang, Y. Hu, L. An and P. Xi, Surface Reconstruction of Covellite CuS Nanocrystals for Enhanced OER Catalytic Performance in Alkaline Solution, *Small*, 2023, **19**(37), 2301762.

26 J. Wu, Y. Zhang, B. Zhang, S. Li and P. Xu, Zn-Doped CoS_2 Nanoarrays for an Efficient Oxygen Evolution Reaction: Understanding the Doping Effect for a Precatalyst, *ACS Appl. Mater. Interfaces*, 2022, **14**(12), 14235–14242.

27 Q. Peng, X. Shao, C. Hu, Z. Luo, T. T. Isimjan, Z. Dou, R. Hou and X. Yang, Co_4S_3 grafted 1 T-phase dominated WS_2 ultrathin nanosheet arrays for highly efficient overall water splitting in alkaline media, *J. Colloid Interface Sci.*, 2022, **615**, 577–586.

28 H. Yin, M. Huang, L. Wang, S. Muhammad, T. T. Isimjan, J. Guo, D. Cai, B. Wang and X. Yang, Lattice-mismatched MOF-on-MOF nanosheets with rich oxygen vacancies show fast oxygen evolution kinetics for large-current water splitting, *Appl. Catal., B*, 2025, **367**, 125105.

29 Q. Peng, Q. He, Y. Hu, T. T. Isimjan, R. Hou and X. Yang, Interface engineering of porous Fe_2P-$WO_{2.92}$ catalyst with oxygen vacancies for highly active and stable large-current oxygen evolution and overall water splitting, *J. Energy Chem.*, 2022, **65**, 574–582.

30 M. Gao, Z. Huang, L. Wang, H. Li, C. Ruan, R. Sadeq, T. T. Isimjan and X. Yang, Synergistic Co-N/V-N dual sites

in N-doped $Co_3V_2O_8$ nanosheets: pioneering high-efficiency bifunctional electrolysis for high-current water splitting, *J. Colloid Interface Sci.*, 2024, **658**, 739–747.

31 F. Wei, J. Shen, J. Gong, Q. Peng, L. Shi, T. T. Isimjan and X. Yang, Oxalic Acid-Assisted Vacancy Engineering Promotes Iron–Copper Sulfide Nanosheets for High-Current Density Water Oxidation, *J. Phys. Chem. Lett.*, 2024, **15**(4), 1172–1180.

32 M. Guo, Z. Huang, Y. Qu, L. Wang, H. Li, T. T. Isimjan and X. Yang, Synergistic effect and nanostructure engineering of three-dimensionally hollow mesoporous spherical Cu_3P/TiO_2 in aqueous/flexible Zn–air batteries, *Appl. Catal., B*, 2023, **320**, 121991.

33 S. Y. Lee, H. Jung, N.-K. Kim, H.-S. Oh, B. K. Min and Y. J. Hwang, Mixed Copper States in Anodized Cu Electrocatalyst for Stable and Selective Ethylene Production from CO_2 Reduction, *J. Am. Chem. Soc.*, 2018, **140**(28), 8681–8689.

34 Y. Jiang, Z. Song, M. Qu, Y. Jiang, W. Luo and R. He, Co—Mn Bimetallic Nanowires by Interfacial Modulation with/without Vacancy Filling as Active and Durable Electrocatalysts for Water Splitting, *Small*, 2024, **20**(33), 2400859.

35 H.-J. Liu, S. Zhang, Y.-N. Zhou, W.-L. Yu, Y. Ma, S.-T. Wang, Y.-M. Chai and B. Dong, Dynamically Stabilized Electronic Regulation and Electrochemical Reconstruction in Co and S Atomic Pair Doped Fe_3O_4 for Water Oxidation, *Small*, 2023, **19**(33), 2301255.

36 Q. Peng, X. Zhuang, L. Wei, L. Shi, T. T. Isimjan, R. Hou and X. Yang, Niobium-Incorporated $CoSe_2$ Nanothorns with Electronic Structural Alterations for Efficient Alkaline Oxygen Evolution Reaction at High Current Density, *ChemSusChem*, 2022, **15**(16), e202200827.

37 L. Wang, M. Xu, H. Li, Z. Huang, L. Wang, T. T. Isimjan and X. Yang, Mn-Doped Zn Metal–Organic Framework-Derived Porous N-Doped Carbon Composite as a High-Performance Nonprecious Electrocatalyst for Oxygen Reduction and Aqueous/Flexible Zinc–Air Batteries, *Inorg. Chem.*, 2023, **62**(33), 13284–13292.

38 E. Zhu, C. Shi, J. Yu, H. Jin, L. Zhou, X. Yang and M. Xu, Simultaneous regulation of thermodynamic and kinetic behavior on FeN_3P_1 single-atom configuration by Fe_2P for efficient bifunctional ORR/OER, *Appl. Catal., B*, 2024, **347**, 123796.

39 C.-H. Chou, C.-H. Yeh, P.-L. Chen, K.-H. Lin, C.-Y. Wu, Z.-C. Yan, P.-H. Hsiao and C.-Y. Chen, Reducing hole-injection hurdles of OER electrocatalysts derived from Ru-doped FeNi metal–organic frameworks anchored with FeOOH, *J. Mater. Chem. A*, 2024, **12**(43), 29526–29537.

40 Z. Huang, Z. Liu, M. Liao, L. Wang, Z. Luo, T. T. Isimjan and X. Yang, Synergistically improved hydrogen evolution by interface engineering of monodispersed $Co_{5.47}N$/CoMoOx hybrid particles on carbon cloth with rich oxygen vacancies, *Chem. Eng. J.*, 2023, **462**, 142281.

41 J. Nai and X. W. Lou, Hollow Structures Based on Prussian Blue and Its Analogs for Electrochemical Energy Storage and Conversion, *Adv. Mater.*, 2019, **31**(38), 1706825.

42 M. Yao, N. Wang, W. Hu and S. Komarneni, Novel hydrothermal electrodeposition to fabricate mesoporous film of $Ni_{0.8}Fe_{0.2}$ nanosheets for high performance oxygen evolution reaction, *Appl. Catal., B*, 2018, **233**, 226–233.

43 Y. Pan, K. Sun, Y. Lin, X. Cao, Y. Cheng, S. Liu, L. Zeng, W.-C. Cheong, D. Zhao, K. Wu, Z. Liu, Y. Liu, D. Wang, Q. Peng, C. Chen and Y. Li, Electronic structure and d-band center control engineering over M-doped CoP (M = Ni, Mn, Fe) hollow polyhedron frames for boosting hydrogen production, *Nano Energy*, 2019, **56**, 411–419.

44 Z. Huang, M. Liao, S. Zhang, L. Wang, M. Gao, Z. Luo, T. T. Isimjan, B. Wang and X. Yang, Valence electronic engineering of superhydrophilic Dy-evoked Ni-MOF outperforming RuO_2 for highly efficient electrocatalytic oxygen evolution, *J. Energy Chem.*, 2024, **90**, 244–252.

45 L. Liu, J. Cao, S. Hu, T. Liu, C. Xu, W. Fu, X. Ma and X. Yang, Antagonism effect of residual S triggers the dual-path mechanism for water oxidation, *J. Energy Chem.*, 2024, **93**, 568–579.

46 L. V. A. Sayson, J. M. Lopez, E. S. Estacio, A. A. Salvador and A. S. Somintac, Nanostructured CuO thin film deposited on stainless steel using spray pyrolysis as supercapacitor electrode, *Mater. Res. Express*, 2020, **6**(12), 125551.

47 J. Huang, B. Hu, Y. Li, J. Zhu, J. Jiang, H. Zhao, J. Zhou, L. Jin and R. Wu, Unveiling the mechanism of enhanced alkaline hydrogen evolution kinetics on molybdenum–cobalt sulfides for efficient anion exchange membrane water electrolyzers, *Inorg. Chem. Front.*, 2025, **12**(17), 5159–5169.

48 T. A. Kumaravelu, T. T. T. Nga, R. R. J, G. J, K. M, W.-C. Chou, J.-L. Chen, C.-L. Chen, B.-H. Lin, C.-H. Du, P.-H. Yeh, A. Kandasami, J.-H. Hsu, C.-C. Wang and C.-L. Dong, Bifunctional NiCo-CuO Nanostructures: A Promising Catalyst for Energy Conversion and Storage, *Small Methods*, 2025, 2401463.

49 H. Su, W. Zhou, W. Zhou, Y. Li, L. Zheng, H. Zhang, M. Liu, X. Zhang, X. Sun, Y. Xu, F. Hu, J. Zhang, T. Hu, Q. Liu and S. Wei, *In situ* spectroscopic observation of dynamic-coupling oxygen on atomically dispersed iridium electrocatalyst for acidic water oxidation, *Nat. Commun.*, 2021, **12**(1), 6118.

50 W. Zhou, H. Su, Z. Wang, F. Yu, W. Wang, X. Chen and Q. Liu, Self-synergistic cobalt catalysts with symbiotic metal single-atoms and nanoparticles for efficient oxygen reduction, *J. Mater. Chem. A*, 2021, **9**(2), 1127–1133.

51 H. Jia, N. Yao, Y. Jin, L. Wu, J. Zhu and W. Luo, Stabilizing atomic Ru species in conjugated sp2 carbon-linked covalent organic framework for acidic water oxidation, *Nat. Commun.*, 2024, **15**(1), 5419.

52 H. Lv, Y. Gao, D.-S. Li, A. Yu, C. Sun and C. Zhang, Mediation of Oxidation and Spin States of Fe/P-CoO_2 Core–Shell Structures Catalysts for Oxygen Evolution Reaction, *Adv. Funct. Mater.*, 2024, 2418334.

53 J. Li, M. Yan, X. Zhou, Z.-Q. Huang, Z. Xia, C.-R. Chang, Y. Ma and Y. Qu, Mechanistic Insights on Ternary $Ni_{2-x}Co_xP$ for Hydrogen Evolution and Their Hybrids with Graphene as Highly Efficient and Robust Catalysts for

Overall Water Splitting, *Adv. Funct. Mater.*, 2016, **26**(37), 6785–6796.

54 L. Wang, Y. Hao, L. Deng, F. Hu, S. Zhao, L. Li and S. Peng, Rapid complete reconfiguration induced actual active species for industrial hydrogen evolution reaction, *Nat. Commun.*, 2022, **13**(1), 5785.

55 J. Hu, A. Al-Salihy, J. Wang, X. Li, Y. Fu, Z. Li, X. Han, B. Song and P. Xu, Improved Interface Charge Transfer and Redistribution in CuO-CoOOH p-n Heterojunction Nanoarray Electrocatalyst for Enhanced Oxygen Evolution Reaction, *Adv. Sci.*, 2021, **8**(22), 2103314.

56 J. Wei, H. Tang, Y. Liu, G. Liu, L. Sheng, M. Fan, Y. Ma, Z. Zhang and J. Zeng, Optimizing the Intermediates Adsorption by Manipulating the Second Coordination Shell of Ir Single Atoms for Efficient Water Oxidation, *Angew. Chem., Int. Ed.*, 2024, **63**(44), e202410520.

57 H. Zhu, S. Sun, J. Hao, Z. Zhuang, S. Zhang, T. Wang, Q. Kang, S. Lu, X. Wang, F. Lai, T. Liu, G. Gao, M. Du and D. Wang, A high-entropy atomic environment converts inactive to active sites for electrocatalysis, *Energy Environ. Sci.*, 2023, **16**(2), 619–628.